

Preprocessed cumulative reconstructor with domain decomposition: a fast wavefront reconstruction method for pyramid wavefront sensor

Iuliia Shatkhina,^{1,*} Andreas Obereder,² Matthias Rosensteiner,² and Ronny Ramlau¹

¹Industrial Mathematics Institute, Johannes Kepler University Linz, Altenbergerstrasse 69, Linz A-4040, Austria

²MathConsult GmbH, Altenbergerstrasse 69, Linz A-4040, Austria

*Corresponding author: iuliia.shatkhina@indmath.uni-linz.ac.at

Received 18 December 2012; revised 11 March 2013; accepted 12 March 2013;
posted 13 March 2013 (Doc. ID 182027); published 15 April 2013

We present a fast method for the wavefront reconstruction from pyramid wavefront sensor (P-WFS) measurements. The method is based on an analytical relation between pyramid and Shack–Hartmann sensor (SH-WFS) data. The algorithm consists of two steps—a transformation of the P-WFS data to SH data, followed by the application of cumulative reconstructor with domain decomposition, a wavefront reconstructor from SH-WFS measurements. The closed loop simulations confirm that our method provides the same quality as the standard matrix vector multiplication method. A complexity analysis as well as speed tests confirm that the method is very fast. Thus, the method can be used on extremely large telescopes, e.g., for eXtreme adaptive optics systems. © 2013 Optical Society of America

OCIS codes: (000.3860) Mathematical methods in physics; (010.7350) Wave-front sensing; (110.1080) Active or adaptive optics; (350.1260) Astronomical optics.

<http://dx.doi.org/10.1364/AO.52.002640>

1. Introduction

Over the past decade, important scientific results were obtained based on observations with 8–10 m class ground-based optical telescopes, equipped with adaptive optics (AO) systems. AO systems compensate the wavefront perturbations caused by the atmospheric turbulence by using deformable mirrors (DMs). In order to push the limits of astronomical observations further, a new generation of extremely large telescopes (ELTs) with primary mirrors over 30 m is currently under development. Such telescopes will allow to observe fainter stars (i.e., will possess an increased sensitivity) and to achieve wide-field images with higher contrast as well as better angular and spatial resolutions.

The direct imaging of extra-solar planets is one of the most challenging fields in modern astronomy because of the huge contrast between the brightness of

the hosting star and of the orbiting planet. For high-contrast imaging at very small angular separations, dedicated exoplanet finding instruments are currently under development for ELTs, e.g., EPICS on the European ELT (E-ELT) [1]. Such instruments will include an eXtreme AO (XAO) system, which is a single conjugate AO (SCAO) system with a very high number of actuators.

A typical AO system consists of three main components: a wavefront sensor (WFS) that measures intensity changes due to the wavefront deformations caused by atmospheric turbulence; a control algorithm that relates the sensor data with the corresponding wavefront shape; and a DM that compensates for the distortions in real time. The classical control approach, known as matrix vector multiplication (MVM), is based on the interaction matrix that maps the mirror commands to sensor measurements. The mirror commands are computed by multiplying the inverse of the interaction matrix (called the control matrix) with a vector containing the measured sensor data [2]. The MVM algorithm

has a complexity of $\mathcal{O}(n^2)$, where n is the number of active DM actuators. In the ELT setting, a huge number (10^4 – 10^5) of actuators need to be controlled at a frequency of about 3 kHz, which makes the application of the MVM method on available real time computer systems rather difficult. Thus, the development of new fast control algorithms is a crucial task for the future successful operation of ELT instruments.

Control (or wavefront reconstruction) algorithms depend on the sensor type that is used in the AO system. Instead of the widely used Shack–Hartmann sensor (SH-WFS), for XAO systems a pyramid wavefront sensor (P-WFS) is suggested due to its increased sensitivity and adjustable pupil sampling. Since the pyramid sensor was introduced by R. Ragazzoni in 1990s [3,4], theoretical studies and numerical simulations have shown the enhanced and adjustable sensitivity as well as a better closed loop performance compared to the SH sensor [5–7]. The advantages of the pyramid over SH sensor were successfully demonstrated on sky [8,9].

The understanding of the physics behind the pyramid sensor has changed over time. In the beginning, the P-WFS was introduced with dynamic modulation of the incoming beam, and described within the geometric optics framework as a slope sensor similar to SH, but with a higher sensitivity [3,5]. Later, the role of the beam modulation was questioned and the pyramid sensor without modulation was studied as well [4]. According to the Fourier optics-based analytical model derived in [10], the nonmodulated P-WFS measures a nonlinear combination of one-dimensional and two-dimensional Hilbert transforms of the incoming light. Then, it was recognized that the dynamic modulation of the beam allows to linearize the sensor and to increase its dynamic range [11]. Taking modulation into account within the Fourier optics framework complicates the nonlinear forward model even more. However, a linearization of the model is possible under certain simplifying assumptions [11,12]. Finally, it was shown that the modulated pyramid sensor measures both the slope and the Hilbert transform of the wavefront, depending on the frequency range and the amount of modulation [11].

There exist already several methods for wavefront reconstruction from P-WFS data. The standard MVM algorithm can handle both the nonmodulated and modulated sensor data, but is too time consuming for the XAO setting. As the interaction matrix is nonsparse, the complexity $\mathcal{O}(n^2)$ of the method cannot be reduced with sparse matrix techniques.

The other two algorithms, which are computationally cheaper than the MVM, are based on approximating the pyramid sensor with two orthogonal roof sensors (R-WFS). For the nonmodulated sensor, the reconstruction method presented in [13] is based on computing the inverse Hilbert transform of the sensor data. It requires the application of one-dimensional Fourier transforms; due to the fast

Fourier transform (FFT), its complexity scales as $\mathcal{O}(n \log n)$.

Another Fourier transform-based reconstructor (FTR) with the complexity $\mathcal{O}(n \log n)$ was developed for the modulated pyramid sensor [14]. However, this method is based on the forward model derived within the geometrical optics framework, which is valid only for large modulations [11]. Simulations of an 8 m telescope have shown that the FTR algorithm provides slightly lower quality than the MVM method, which may be nonnegligible in the ELT setting [14]. Therefore, so far there exists no algorithm able to handle both the nonmodulated and modulated pyramid sensor data within the XAO real time requirements.

In this paper we present a new method that satisfies both conditions. Our approach is based on the relation between the pyramid and SH sensor in the Fourier domain. Using this relation, we derive a preprocessing step that transforms the pyramid data into SH-like data, and then apply the *cumulative reconstructor with domain decomposition (CuReD)* developed for SH sensor [15–17]. Our two-step method is called P-CuReD, which stands both for the *preprocessed CuReD* and the *CuReD for pyramid WFS*. The closed loop simulation results show that our method provides the same quality as the MVM method but is much faster. Both the data preprocessing step and the application of the CuReD are computationally very efficient. The whole algorithm has a linear complexity, is highly parallelizable and pipelinable, which makes the method attractive for XAO applications.

In Section 2 we shortly explain the physics of the pyramid sensor and summarize the existing theoretical models. The necessary details like the roof sensor approximation, closed loop linearization, and beam modulation are described therein as well. Section 3 provides the theoretical background of our method, which consists of two steps—the data preprocessing and the reconstruction step. Details concerning the theory and practical implementation of the data preprocessing step are provided in Section 4. The second component of our approach, the CuReD method, is described in Section 5. In Section 6 the closed loop performance of our algorithm is compared to the MVM results. Properties of the P-CuReD method with respect to noise propagation are discussed in Section 7. The computational complexity and the speed of our method are estimated in Section 8.

2. Pyramid WFS

As one can see from Fig. 1, the main component of the pyramid sensor is a four-sided glass pyramidal prism placed in the focal plane of the telescope pupil. The incoming light is focused by the telescope onto the prism apex. The four facets of the pyramid split the incoming light in four beams, propagating in slightly different directions. A relay lens placed behind the prism re-images the four beams, allowing adjustable sampling of the four different images I_i ,

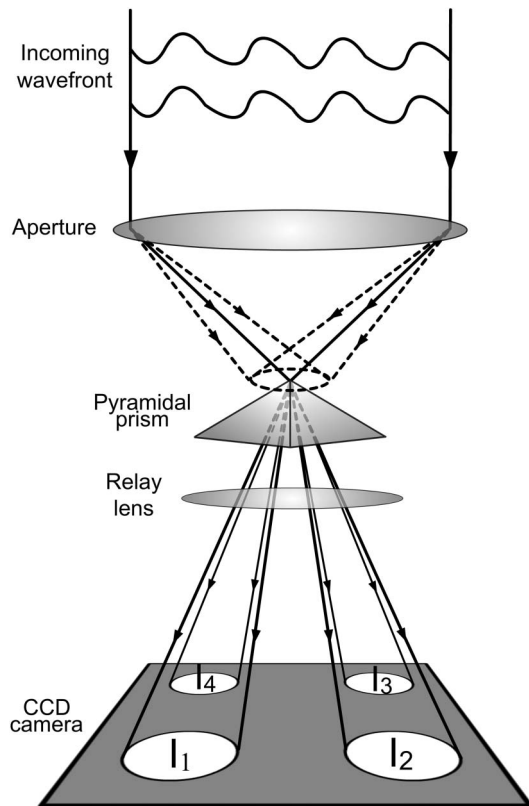


Fig. 1. Scheme of an optical setup of a pyramid WFS. The circular modulation path is shown in the dashed line.

$i = \{1, 2, 3, 4\}$, of the aperture on the CCD camera. The two measurement sets S_x, S_y are obtained from the four intensity patterns [11,12] as

$$S_x(x, y) = \frac{[I_1(x, y) + I_2(x, y)] - [I_3(x, y) + I_4(x, y)]}{I_0}, \quad (1)$$

$$S_y(x, y) = \frac{[I_1(x, y) + I_4(x, y)] - [I_2(x, y) + I_3(x, y)]}{I_0}, \quad (2)$$

where I_0 is the average intensity per subaperture. Dynamic modulation of the incoming beam allows to increase the linear range of the pyramid sensor [11] and is also used to adjust its sensitivity. The modulation can be accomplished in several ways: either by oscillating the pyramid itself [3], with a steering mirror [12,18] or by using a static diffusive optical element [18]. Two modulation scenarios—linear and circular—are usually considered in the literature. The circular modulation path of the focused beam on the pyramid apex is shown with a dashed circle in Fig. 1.

The full Fourier optics-based forward model of the nonmodulated P-WFS, derived in [10], is mathematically difficult to invert. The sensor measures a combination of one-dimensional and two-dimensional Hilbert transforms of the nonlinear functions of the phase [10]. For the modulated pyramid sensor, the theoretical model becomes even more complicated.

However, several assumptions allow to simplify the forward model significantly. In the remainder of the section we will focus on these assumptions and the corresponding approximate models.

A. Roof WFS Approximation

The theoretical model of the P-WFS becomes simpler when the four-sided pyramidal prism is substituted with two orthogonally placed two-sided roof prisms [11–13]. Each roof provides two different images of the aperture on the detector. The two data sets S_x, S_y are obtained as the difference between the two intensity patterns. Due to the physical decoupling of the prisms and their orthogonal placement with respect to each other, the two signal sets S_x and S_y are independent and contain information about the phase ϕ only in x - and only in y -direction correspondingly. Under the roof assumption, the nonmodulated P-WFS signal S_x^n is approximated as

$$S_x^n(x, y) = \frac{1}{\pi} \int_{-B(y)}^{+B(y)} \frac{\sin[\phi(x', y) - \phi(x, y)]}{x - x'} dx', \quad (3)$$

where $B(y)$ denotes the boundary of the pupil images for a fixed y . Due to the symmetry of the two identical roofs, the measurements S_y are similar. Thus we will consider only one set of measurements S_x , but keep in mind that all the theory works in the same way for the S_y signal.

For a linear modulation with amplitude $\alpha = (b\lambda/D)$ with a positive integer b , the pyramid sensor signal S_x^l is approximated [11,12] by

$$S_x^l(x, y) = \frac{1}{\pi} \int_{-B(y)}^{+B(y)} \frac{\sin[\phi(x', y) - \phi(x, y)]}{x - x'} \times \text{sinc}(\alpha_\lambda(x - x')) dx', \quad (4)$$

where $\alpha_\lambda = (2\pi\alpha/\lambda)$. Note that we keep the notations as in [11], but change the sign in the denominator.

For a circular modulation of the same amplitude α , the P-WFS measurement S_x^c is given [12] as

$$S_x^c(x, y) = \frac{1}{\pi} \int_{-B(y)}^{+B(y)} \frac{\sin[\phi(x', y) - \phi(x, y)]}{x - x'} \times J_0(\alpha_\lambda(x - x')) dx', \quad (5)$$

where J_0 denotes the zero-order Bessel function of the first kind.

B. Closed Loop Approximation

Further simplification of the theoretical models is possible under the two additional assumptions of an infinite telescope size $B(y) \rightarrow \infty$ and small wavefront distortions $\phi \ll 1$ (as expected in the closed loop). As for a small phase ϕ holds $\sin \phi \simeq \phi$, these assumptions allow to approximate the pyramid sensor measurements with linearized models. For the nonmodulated case, the measurements S_x^n are given as the Hilbert transform of the phase ϕ

$$S_x^n(x, y) = -\phi(x, y) * \frac{1}{\pi x} = -\mathcal{H}\phi. \quad (6)$$

Here, $*$ denotes the convolution operator. For linear modulation, the P-WFS measurements S_x^l are given [11] as

$$S_x^l(x, y) = -\phi(x, y) * \frac{\text{sinc}(\alpha_\lambda x)}{\pi x}. \quad (7)$$

For circular modulation the P-WFS measurements S_x^c are approximated by

$$S_x^c(x, y) = -\phi(x, y) * \frac{J_0(\alpha_\lambda x)}{\pi x}. \quad (8)$$

The wavefront reconstruction method presented in this paper will be based on these linearized models.

3. Data Preprocessing: Transformation to SH Data

Our wavefront reconstruction approach consists of two steps: first, we transform the P-WFS measurements into SH-like data using the analytical Fourier domain filters corresponding to these two sensors; then, to the modified data we apply any of the existing algorithms for wavefront reconstruction from the SH data. The chosen algorithm for the second step is the *CuReD*, see Section 5. In this section we present the theoretical background for the data preprocessing step.

Due to the symmetry between the measurements S_x and S_y , we present the theory for the generalized measurements, which we denote by S_{pyr} . According to [11], the linearized pyramid sensor with linear modulation behaves in the Fourier domain as

$$(\mathcal{F}S_{\text{pyr}}^l)(u) = (\mathcal{F}\phi)(u) \cdot g_{\text{pyr}}^l(u) \cdot \text{sinc}(du) \quad (9)$$

with the filter g_{pyr}^l derived from Eq. (7) as

$$g_{\text{pyr}}^l(u) = \begin{cases} i \text{sgn}(u), & |u| > u_{\text{mod}}, \\ iu/u_{\text{mod}}, & |u| \leq u_{\text{mod}}, \end{cases} \quad (10)$$

where u denotes the spatial frequency sampled in the interval $[-u_{\text{cut}}, u_{\text{cut}}]$ with sampling size $u_{\text{step}} := 1/D$, $u_{\text{cut}} = 1/(2d)$ is the cutoff frequency, D is the telescope diameter, $d = D/\sqrt{n_s}$ is the sensor subaperture size defined by the number n_s of subapertures, the parameter $u_{\text{mod}} > 0$ is defined as $u_{\text{mod}} = a/\lambda = b/D$, and b is a positive integer.

The S-H sensor is described [11] in the Fourier domain as

$$(\mathcal{F}S_{\text{sh}})(u) = (\mathcal{F}\phi)(u) \cdot g_{\text{sh}}(u) \cdot \text{sinc}(du) \quad (11)$$

with the filter function g_{sh} given as

$$g_{\text{sh}}(u) = 2i\pi du. \quad (12)$$

For pyramid sensor without and with circular modulation, the Fourier domain relation (9) holds

with different filter functions, g_{pyr}^n and g_{pyr}^c correspondingly. In the nonmodulated case, the Fourier domain filter g_{pyr}^n is derived from Eq. (6) as

$$g_{\text{pyr}}^n(u) = i \text{sgn}(u), \quad \forall u \in [-u_{\text{cut}}, u_{\text{cut}}]. \quad (13)$$

And in the circular modulation case, the Fourier filter g_{pyr}^c is derived from Eq. (8) (see Appendix A) as

$$g_{\text{pyr}}^c(u) = \begin{cases} i \text{sgn}(u), & |u| > u_{\text{mod}}, \\ \frac{2i}{\pi} \arcsin(u/u_{\text{mod}}), & |u| \leq u_{\text{mod}}. \end{cases} \quad (14)$$

Therefore, for any modulation scenario, we can derive a Fourier domain relation between the two sensors as

$$(\mathcal{F}S_{\text{sh}})(u) = (\mathcal{F}S_{\text{pyr}})(u) \cdot g_{\text{sh/pyr}}(u), \quad (15)$$

where the SH to pyramid data transmission filter $g_{\text{sh/pyr}}$ is defined as

$$g_{\text{sh/pyr}}(u) := \frac{(\mathcal{F}S_{\text{sh}})(u)}{(\mathcal{F}S_{\text{pyr}})(u)} = \frac{g_{\text{sh}}(u)}{g_{\text{pyr}}(u)}. \quad (16)$$

According to the Fourier convolution theorem, we derive the corresponding relation between the two sensors in the space domain as

$$S_{\text{sh}}(x) = \frac{1}{\sqrt{2\pi}} S_{\text{pyr}}(x) * p_{\text{sh/pyr}}(x), \quad (17)$$

where the kernel $p_{\text{sh/pyr}}(x)$ is obtained by computing the inverse Fourier transform (IFT) of the SH to pyramid data transmission filter $g_{\text{sh/pyr}}$ as

$$p_{\text{sh/pyr}}(x) := (\mathcal{F}^{-1}g_{\text{sh/pyr}})(x). \quad (18)$$

Hence, the data preprocessing step consists in the row-wise convolution of the pyramid sensor data S_x with the one-dimensional kernel $p_{\text{sh/pyr}}$, and the column-wise convolution of S_y with the same kernel. Theoretical details about the computation of the kernel $p_{\text{sh/pyr}}(x)$ as well as its practical implementation are given in Section 4.

4. Space Domain Kernel

Based on the Fourier domain filter functions $g_{\text{pyr}}^{n,l,c}$ and g_{sh} introduced above, in this section we first derive the three SH to pyramid data transmission filters $g_{\text{sh/pyr}}^{n,l,c}$, and then compute the corresponding space domain kernels $p_{\text{sh/pyr}}^{n,l,c}$.

The SH/pyramid transmission filter $g_{\text{sh/pyr}}^n$ in the nonmodulated case is given as

$$g_{\text{sh/pyr}}^n(u) = 2\pi du \text{sgn}(u), \quad \forall u \in [-u_{\text{cut}}, u_{\text{cut}}] \quad (19)$$

with

$$\begin{aligned} \lim_{u \rightarrow 0} g_{\text{sh/pyr}}^n(u) &= \lim_{u \rightarrow 0} \frac{g_{\text{sh}}(u)}{g_{\text{pyr}}^n(u)} = \lim_{u \rightarrow 0} \frac{2i\pi du}{i \operatorname{sgn}(u)} \\ &= \lim_{u \rightarrow 0} \frac{2i\pi d |u| \operatorname{sgn}(u)}{i \operatorname{sgn}(u)} = \lim_{u \rightarrow 0} 2i\pi d |u| = 0. \end{aligned}$$

In the linear modulation case, the transmission filter $g_{\text{sh/pyr}}^l$ is

$$g_{\text{sh/pyr}}^l(u) = \begin{cases} 2\pi du \operatorname{sgn}(u), & |u| > u_{\text{mod}}, \\ 2\pi du_{\text{mod}}, & |u| \leq u_{\text{mod}}, \end{cases} \quad (20)$$

with

$$\begin{aligned} \lim_{u \rightarrow 0} g_{\text{sh/pyr}}^l(u) &= \lim_{u \rightarrow 0} \frac{g_{\text{sh}}(u)}{g_{\text{pyr}}^l(u)} = \lim_{u \rightarrow 0} \frac{2i\pi du u_{\text{mod}}}{iu} \\ &= 2\pi du_{\text{mod}}. \end{aligned}$$

And in the circular modulation case, the transmission filter $g_{\text{sh/pyr}}^c$ equals

$$g_{\text{sh/pyr}}^c(u) = \begin{cases} 2\pi du \operatorname{sgn}(u), & |u| > u_{\text{mod}}, \\ \frac{\pi^2 du}{\arcsin(u/u_{\text{mod}})}, & |u| \leq u_{\text{mod}}, \end{cases} \quad (21)$$

where with L'Hôpital rule we obtain

$$\begin{aligned} \lim_{u \rightarrow 0} g_{\text{sh/pyr}}^c(u) &= \lim_{u \rightarrow 0} \frac{g_{\text{sh}}(u)}{g_{\text{pyr}}^c(u)} = \lim_{u \rightarrow 0} \frac{2i\pi^2 du}{2i \arcsin(u/u_{\text{mod}})} \\ &= \lim_{u \rightarrow 0} \frac{(\pi^2 du)'_u}{(\arcsin(u/u_{\text{mod}}))'_u} \\ &= \lim_{u \rightarrow 0} \pi^2 d \sqrt{u_{\text{mod}}^2 - u^2} = \pi^2 du_{\text{mod}}. \end{aligned}$$

Figure 2 shows the three transmission filters $g_{\text{sh/pyr}}^{n,l,m}$ corresponding to the following XAO settings: telescope diameter $D = 42$ m, $n_s = 200 \times 200$ subapertures, modulation amplitude (where applicable) $\alpha = 4\lambda/D$.

The space domain kernel $p_{\text{sh/pyr}}^n$ corresponding to the nonmodulated case is equal, as shown in Appendix B, to

$$\begin{aligned} p_{\text{sh/pyr}}^n(x) &= 4\pi du_{\text{cut}}^2 \operatorname{sinc}(2xu_{\text{cut}}) \\ &\quad - 2\pi du_{\text{cut}}^2 \operatorname{sinc}^2(xu_{\text{cut}}). \end{aligned} \quad (22)$$

In the linear modulation case, as shown in Appendix C, the space domain kernel $p_{\text{sh/pyr}}^l$ equals

$$\begin{aligned} p_{\text{sh/pyr}}^l(x) &= 4\pi du_{\text{cut}}^2 \operatorname{sinc}(2xu_{\text{cut}}) \\ &\quad + 2\pi du_{\text{mod}}^2 \operatorname{sinc}^2(xu_{\text{mod}}) \\ &\quad - 2\pi du_{\text{cut}}^2 \operatorname{sinc}^2(xu_{\text{cut}}). \end{aligned} \quad (23)$$

Figure 3 shows the analytically computed space domain kernel $p_{\text{sh/pyr}}^l(x)$, $x \in \Omega = [-D/2, D/2]$

SH/pyramid transmission filters in the Fourier domain

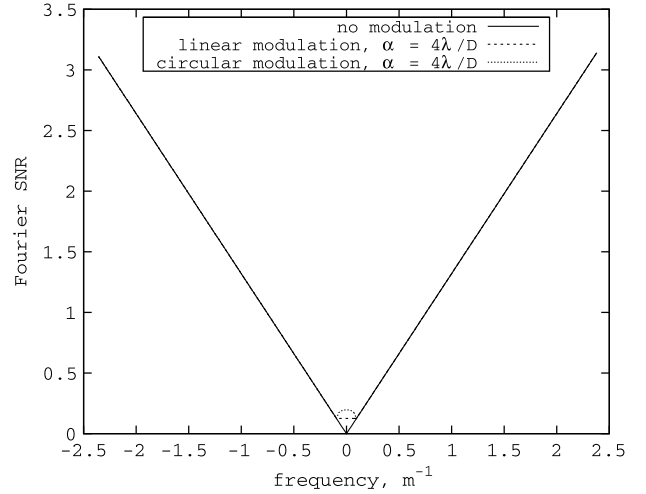


Fig. 2. SH to pyramid data transmission filters $g_{\text{sh/pyr}}^{n,l,m}$ in the Fourier domain corresponding to the following AO system parameters: telescope diameter $D = 42$ m, number of WFS subapertures $n = 200$, modulation amplitude (where applicable) $4\lambda/D$. The difference between the three filters is only in the low frequency domain.

corresponding to the modulation amplitude $\alpha = 4\lambda/D$. For circular modulation the analytical expression for $p_{\text{sh/pyr}}^c$ is not available, however it can be computed numerically by using the FFT.

As the sensor measurements $S_x(x, \cdot)$ depend on the discretized space variable $x \in \Omega = [-D/2, D/2]$, where the domain Ω is sampled with the step size d , we need to find a discrete representation of the kernels $p_{\text{sh/pyr}}^{n,l}$ that would fit the sensor data. Several possibilities are available. First of all, we can discretize the kernels $p_{\text{sh/pyr}}^{n,l}$ by averaging the kernel values over the subapertures. Another way to get the discretized kernels is to use the discrete domain

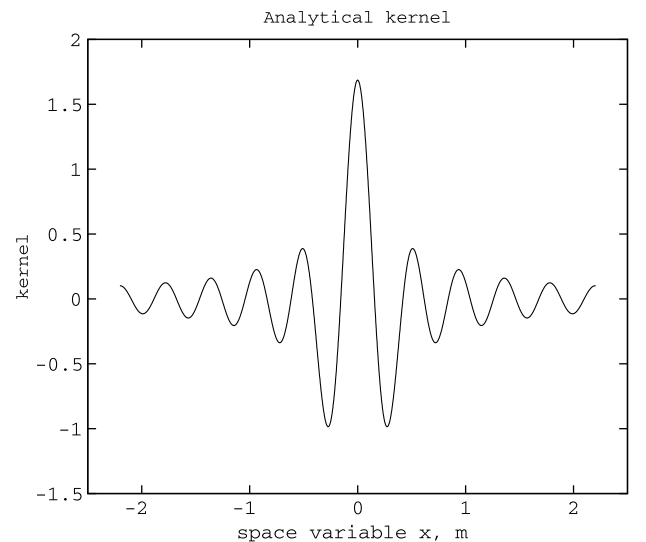


Fig. 3. Analytical space domain kernel $p_{\text{sh/pyr}}^l$ corresponding to the following AO system parameters: telescope diameter $D = 42$ m, number of WFS subapertures $n_s = 200 \times 200$, linear modulation with amplitude $4\lambda/D$.

$\bar{\Omega}$ when computing the analytical expressions (22,23). Finally, the kernels $p_{sh/pyr}^{n,l,c}$ can be computed numerically by using the FFT routine.

The three discretization approaches are compared in Fig. 4 for the space domain kernel $p_{sh/pyr}^l$ corresponding to linear modulation with amplitude $\alpha = 4\lambda/D$. As one can see, the last two approaches lead to the identical result, and the first approach gives a similar result.

It is important to note that for the small modulation amplitude $4\lambda/D$, the numerically computed kernels $p_{sh/pyr}^l$ and $p_{sh/pyr}^c$, corresponding to linear and circular modulation, practically coincide. The difference between the two kernels is of the order of 10^{-3} , hence negligible for our needs. However, for larger modulation amplitudes the difference between $p_{sh/pyr}^l$ and $p_{sh/pyr}^c$ increases.

The quality test results presented in Section 6 were obtained with the kernels $p_{sh/pyr}^{n,c}$ computed numerically with the FFT routine. Note that the discretized kernels $p_{sh/pyr}^{n,c}$ have very few nonzero values. Therefore, the data preprocessing step that consists in convolving the WFS measurements row-wise and column-wise with the kernels $p_{sh/pyr}^{n,c}$ is very efficient from the computational point of view (for details see Section 8).

5. Wavefront Reconstruction from Preprocessed Data: CuReD

The data preprocessing step transforms the pyramid sensor measurements into SH like data. Therefore, we need to apply an algorithm used for reconstruction of the wavefront from these measurements. According to the mathematical model, the SH

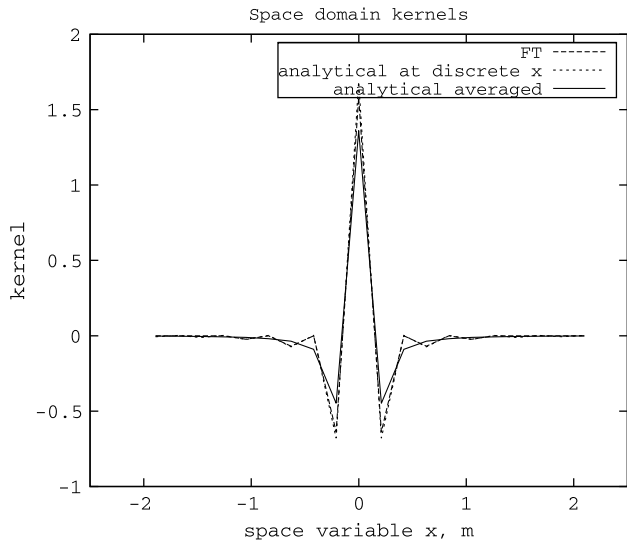


Fig. 4. Discretized space domain kernel $p_{sh/pyr}^l$ computed in three different ways: using the FFT routine (large dashed line); with the analytical formula evaluated at a discretized grid (small dashed line); and by averaging the analytical formula over subapertures (solid line). The kernels correspond to the following AO system parameters: telescope diameter $D = 42$ m, number of WFS subapertures $n_s = 200 \times 200$, linear modulation with amplitude $4\lambda/D$.

sensor measures wavefront gradients, averaged over the subapertures.

There are numerous algorithms that reconstruct the wavefront from these measurements and all of them could be used in combination with the preprocessing step to solve the reconstruction problem for the P-WFS. As in an XAO system the resolution of the sensor and the frequency of the system are especially high, the requirements with respect to computational speed on a reconstruction algorithm are demanding. We propose to use the *CuReD*, as this method reconstructs the wavefront accurately and is extremely fast (it needs only $20n_s$ operations, where n_s is number of the sensor subapertures) as well as parallelizable and pipelineable. It was introduced in [17] and adapted to real life telescope geometries in [15]. The domain decomposition for the reduction of the noise propagation is presented in [16]. The *CuReD* algorithm was used as the second step of our method to obtain the test results in Section 6.

6. Closed Loop Performance

To test the quality of our reconstruction method in a closed loop setting, we use the end-to-end simulator OCTOPUS provided by the European Southern Observatory (ESO) [19]. The used simulation parameters are summarized in Table 1. We consider an XAO system with telescope diameter of $D = 42$ m and a pyramid sensor. The software simulates a nine-layer atmospheric model, each layer being a random realization of the von Karman power spectrum.

We consider three test cases (A, B, C), summarized in Table 2. Test cases A and B deal with a 200×200 pyramid sensor (meaning a sensor with 200×200 subapertures) with (A) and without (B) circular modulation correspondingly, while in case C we consider an 84×84 pyramid sensor without modulation. The large-scale XAO system (cases A and B) runs at a frequency of 3 kHz, while the smaller AO system (test case C) is running at 1 kHz.

For the temporal control of the closed loop we use a simple integrator, the gain is optimized manually. The used quality metrics are the long-exposure

Table 1. Simulation Parameters

Telescope diameter D	42 m
Central obstruction	28%
Science target	On-axis (SCAO)
Science band	$K, \lambda_{\text{Strehl}} = 2200$ nm
Sensing band	$R, \lambda_{\text{WFS}} = 700$ nm
WFS	Pyramid
Type of modulation	Circular
Controller	Integrator
Atmospheric model	von Karman
Number of simulated layers	9
Outer scale L_0	25 m
Fried radius r_0 at $\lambda = 500$ nm	
For good atmosphere	0.172 m
For median atmosphere	0.129 m
For bad atmosphere	0.094 m

(LE) Strehl ratio and the corrected point spread function (PSF). In the following we present the performance results separately for each of the three test cases.

A. Test Case A

First, we test the closed loop performance of our reconstruction method for a 200×200 pyramid sensor with the modulation radius $\alpha = 4\lambda/D$. We evaluate the quality in a wide range of atmospheric conditions and photon flux levels as given in Table 2. The photon flux levels are indicated by the number of photons per subaperture per frame. For the definition of the good, median, and bad atmosphere via the Fried radius see Table 1. The loop gain for the temporal control is optimized (on 100 time steps) for each photon flux level with a resolution of 0.1. The results are obtained simulating 500 time steps. Higher-order DM influence functions are assumed.

We compare the quality of our method with the results achieved by the MVM method, which were provided to us by ESO. Table 3 gives a comparison of the LE Strehl ratios obtained with the two methods for three “ESO-standard atmospheres” and varying photon flux. The result obtained for the median atmosphere is visualized in Fig. 5. It shows that our method achieves the same quality in the high photon flux case, and a slightly better quality in the low flux case. In Fig. 6 we compare the PSFs in the K -band for the median atmosphere obtained with our reconstructor (P-CuReD) and with the MVM method for the high-flux case (1e4 photons/subaperture/frame). It shows that the PSFs obtained with the two approaches are very similar apart from the high frequency domain.

Hence, the quality achieved with our two-step approach is comparable to or slightly better than the quality obtained with the MVM method.

Additionally, Fig. 7 illustrates the convergence rate of P-CuReD compared to that of the MVM method. It shows the simulated SE Strehl ratio in K band obtained with two wavefront reconstruction methods using the parameters for the test case A, median atmosphere and high photon flux level (1e4 photons/subaperture/frame). As one can see, the P-CuReD converges slightly faster than the MVM method. One should remark that, for the sake

of reducing the computational effort, the CuReD algorithm without any data preprocessing was used in the first seven AO loops.

B. Test Case B

The next set of tests evaluates the performance of the P-CuReD for a 200×200 pyramid sensor without modulation. The quality is evaluated for the median atmosphere and varying photon flux. The loop gain for the temporal control is optimized (on 100 time steps) for each photon flux level with a resolution of 0.1. The results are obtained simulating 1000 time steps. Higher-order DM influence functions are assumed.

The LE Strehl ratios obtained with our reconstruction method are plotted in Fig. 8. Up to our knowledge, for this XAO setting there are no reported quality tests of other methods. Thus, in order to compare the performance of our wavefront reconstructor in the nonmodulated sensor case with the MVM method, test case C is designed and performed.

C. Test Case C

The last tested configuration is a telescope with diameter of 42 m and a nonmodulated pyramid sensor with 84×84 subapertures. We compare the performance of our approach to the MVM results from [20]. We evaluate the quality for the median atmosphere and high photon flux (1e4 photons/subaperture/frame). The loop gain for the temporal control is optimized (on 200 time steps) with a resolution of 0.1. The results are obtained simulating 1000 time steps. Bilinear DM influence functions are assumed in this test case. The P-CuReD provides the LE Strehl ratio of 0.71, the corresponding MVM result is 0.43.

7. Noise Propagation

In this section, we analyze the properties of the P-CuReD method with respect to propagation of white noise, independent for each subaperture. Since the preprocessing of the pyramid sensor data is linear, it can be represented as an MVM. We denote the corresponding matrix by P . According to [15], the CuReD algorithm is linear as well, and can be represented by a matrix C . Therefore, the matrix $M = CP$ is equivalent to the P-CuReD method.

Table 2. Test Case Parameters

Test Case	A and B		C
Number of subapertures n_s	200 × 200		84 × 84
Number of active subapertures	28,800 out of 40,000		5040 out of 7056
Frame rate	3 kHz		1 kHz
DM delay	1		2
Influence functions	Higher order		Bilinear spline
Photon flux	[5, 10, 50, 100, 1000, 10,000]		10,000
Test case	A	B	C
Modulation radius in λ/D	4	0	0
Atmosphere	[good, median, bad]	Median	Median
Iterations per simulation	500	1000	1000

Table 3. Comparison of the LE Strehl Ratios Obtained with the MVM Method and with the P-CuReD for Different Atmospheres and Photon Fluxes Using the Parameters Defined in Test Case A

Atmosphere	Good		Median		Bad	
Photon flux	MVM	P-CuReD	MVM	P-CuReD	MVM	P-CuReD
5	0.8709	0.9317	0.7260	0.8969	0.4355	0.8203
10	0.9524	0.9582	0.9261	0.9380	0.8785	0.9006
50	0.9742	0.9748	0.9585	0.9607	0.9260	0.9344
100	0.9765	0.9766	0.9621	0.9630	0.9335	0.9378
1000	0.9785	0.9780	0.9651	0.9649	0.9384	0.9405
10,000	0.9788	0.9781	0.9654	0.9650	0.9387	0.9408

The noise propagation of the P-CuReD method is estimated by the mean squared error (mse) as

$$\text{mse} = \frac{\text{tr}(\mathbf{M}\mathbf{M}^T)}{n}, \quad (24)$$

where tr denotes the trace of a matrix, and n denotes the number of actuators.

To illustrate the noise propagation properties of our method, we have performed several tests. First, we fix a telescope diameter $D = 42$ m and a modulation amplitude $\alpha = 4\lambda/D$, and vary the number of subapertures n_s (hence, the subaperture size d) and the level of subdivisions in the CuReD algorithm. In this configuration, the frequency sampling size u_{step} and the parameter u_{mod} are fixed, while the cutoff frequency u_{cut} grows with the number of subapertures n_s . For larger n_s , the frequency range, for which the pyramid sensor acts as a slope sensor, becomes relatively smaller. The obtained estimates of noise propagation are shown in Fig. 9. As one can see, the mse increases with the number of actuators, however by increasing the number of subdivisions in the CuReD algorithm, one can reduce the mse significantly.

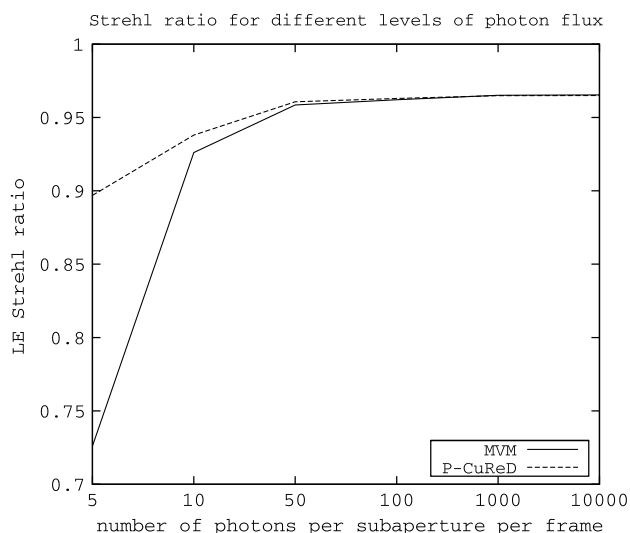


Fig. 5. Simulated LE Strehl in K band obtained with the P-CuReD and with the MVM method using the parameters for the test case A and median atmosphere versus the detected natural guide star (NGS) photon flux.

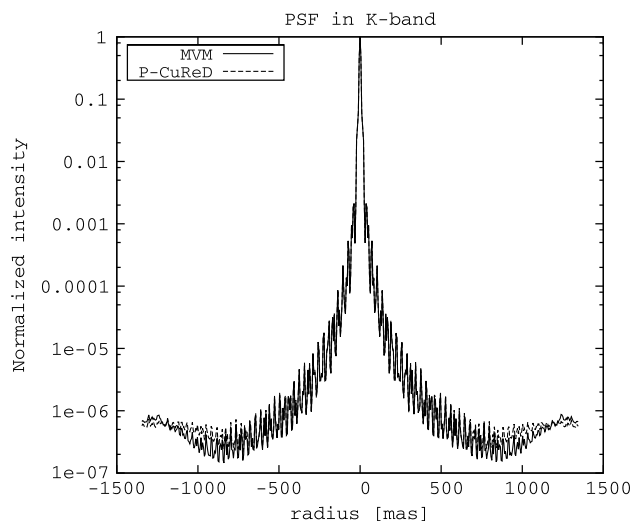


Fig. 6. Simulated LE PSF in K band obtained with the P-CuReD and with the MVM method using parameters for the test case A, median atmosphere and high photon flux level (1e4 photons/subaperture/frame). The two PSFs are equal up to approximately 800 mas.

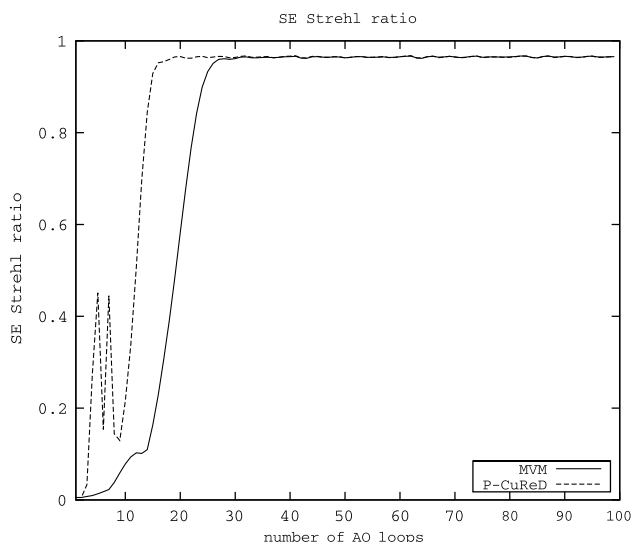


Fig. 7. Simulated SE Strehl in K band obtained with the P-CuReD and with the MVM method using the parameters for the test case A, median atmosphere and high photon flux level (1e4 photons/subaperture/frame).

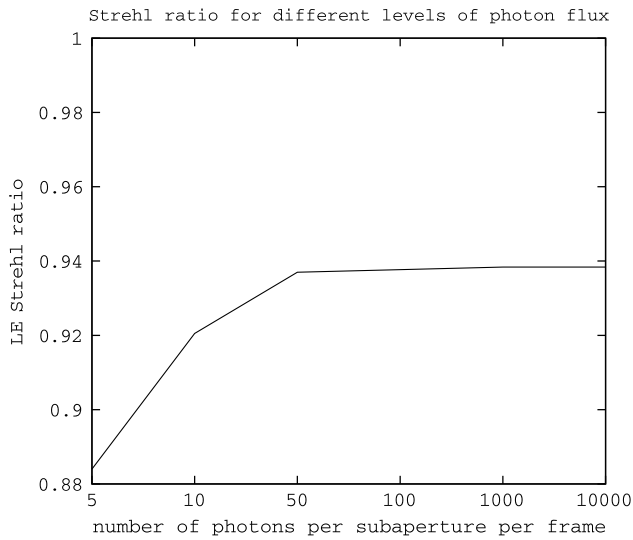


Fig. 8. Simulated LE Strehl in *K* band obtained with the P-CuReD method using parameters for the test case B versus the detected NGS photon flux.

Second, we fix a subaperture size $d = 0.21$ m, and a modulation amplitude $\alpha = 4\lambda/D$, and vary the number of subapertures n_s (hence, the telescope diameter D) and the level of subdivisions in the CuReD algorithm. In this configuration, the cutoff frequency u_{cut} is fixed, while the frequency sampling size u_{step} and the parameter u_{mod} decrease when the number of subapertures n_s increases. For larger n_s , the frequency range, for which the pyramid sensor acts as a slope sensor, becomes relatively smaller. As one can see in Fig. 10, the mse stays at the same level, which is again lower for a larger number of subdivisions in the CuReD algorithm.

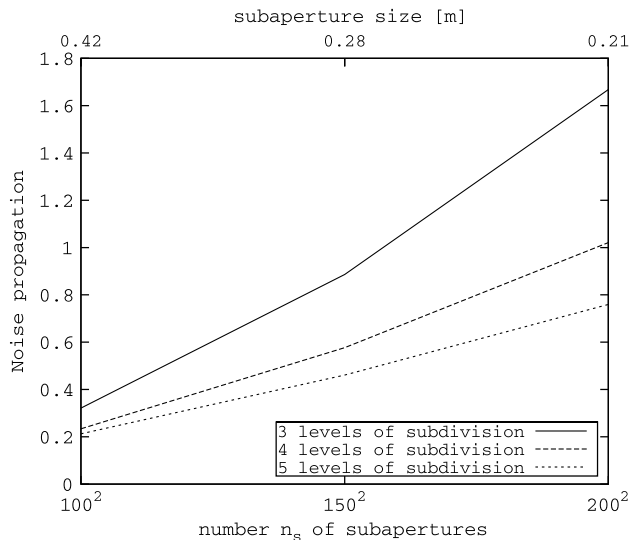


Fig. 9. Noise propagation of the P-CuReD method for annular aperture of a fixed diameter $D = 42$ m and different number of sensor subapertures n_s (and correspondingly the subaperture sizes d). Modulation amplitude $\alpha = 4\lambda/D$ is assumed. The results are shown for three different levels of subdivision in the CuReD algorithm.

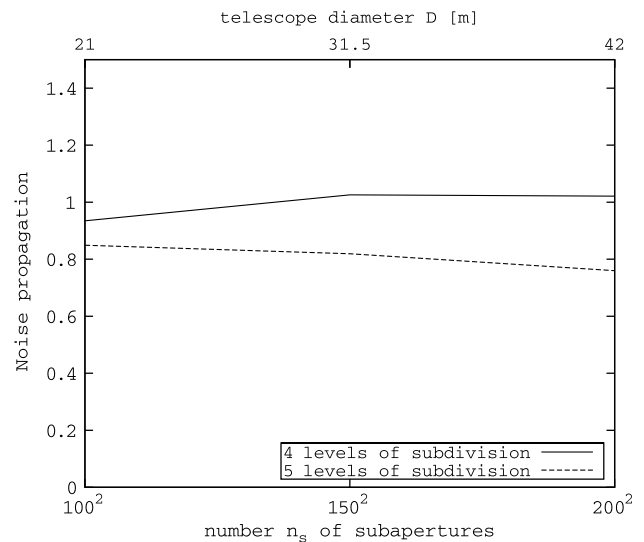


Fig. 10. Noise propagation of the P-CuReD method for annular apertures of different diameters and a fixed subaperture size $d = 0.21$ m. The number n_s of sensor subapertures changes correspondingly. Modulation amplitude $\alpha = 4\lambda/D$ is assumed. The results are shown for two different levels of subdivision in the CuReD algorithm.

Third, we fix the telescope diameter $D = 42$, the subaperture size $d = 0.21$ m, the number of subapertures $n_s = 200 \times 200$, and vary the modulation amplitude α . In this configuration, the cutoff frequency u_{cut} and the frequency sampling size u_{step} are fixed. The relative range where the pyramid sensor acts as a slope sensor increases with the parameter u_{mod} . However, as one can see from Fig. 11, the mse seems to be optimal for a small modulation amplitude $\alpha = 4\lambda/D$, and grows with increasing α . Again,

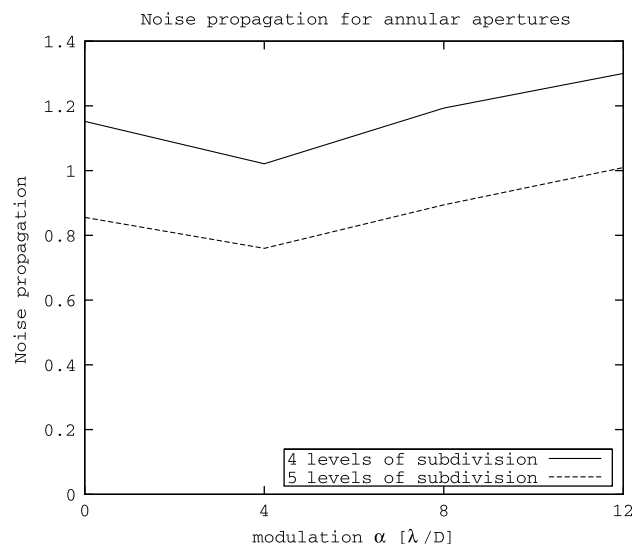


Fig. 11. Noise propagation of the P-CuReD method for annular apertures of the fixed diameter $D = 42$ m, subaperture size $d = 0.21$ m, and number of sensor subapertures $n_s = 200 \times 200$ and varying modulation amplitudes α . The results are shown for two different levels of subdivision in the CuReD algorithm.

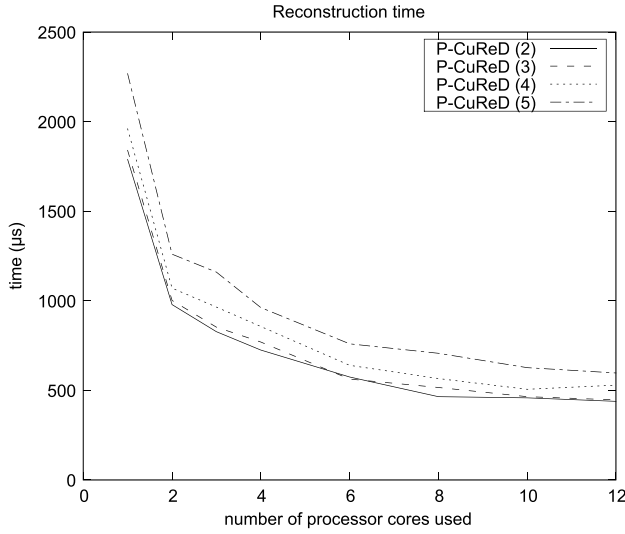


Fig. 12. Reconstruction times obtained with the P-CuReD (k) algorithm for an XAO system with a 200×200 pyramid WFS. Here k indicates the number of subdivisions in the CuReD algorithm [16].

more levels of subdivision in the CuReD method allow to reduce the noise propagation significantly.

8. Complexity and Speed

The first step of our method, the data preprocessing, consists in the row-wise convolution of S_x and column-wise convolution of S_y with a c -point filter, where c is a small integer. For instance, $c = 7$ for the XAO settings tested in Section 6. Hence, the number of operations needed for the data preprocessing step is $\sqrt{n_s} \cdot (c + (c - 1)) \cdot \sqrt{n_s} \cdot 2 = (4c - 2)n_s$, where n_s denotes the number of active sensor subapertures. The second step, application of the CuReD algorithm, requires $20n_s$ operations [16]. Therefore, the whole method (P-CuReD) has a linear complexity $\mathcal{O}(n_s)$. Both steps of the method are parallelizable and pipelinable.

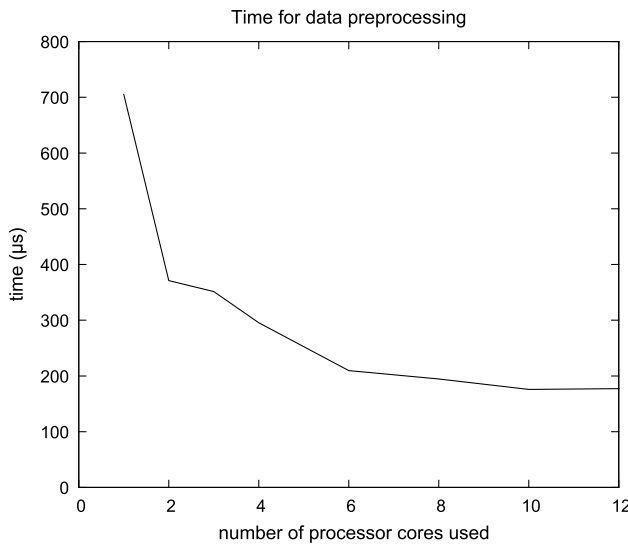


Fig. 13. Computation time for applying the data preprocessing step to the 200×200 pyramid WFS measurements.

The prototype was tested on a computer with 2 Intel hexacore processors, so with a total number of 12 processor cores available, running at a speed of 2.66 GHz. The code is not specialized to any specific aperture geometry. The parallelization was tested with openMP and in the figures the minimal runtime of the algorithm is given. Figure 12 shows the reconstruction times for the full XAO system (for different levels of subdivision in the CuReD algorithm), whereas Fig. 13 shows the standalone runtime of the data preprocessing step.

For a comparison, we tested the MVM method on the same machine and obtained the minimal runtime of 402 ms. This shows that the CuReD with the data preprocessing is indeed much faster than the MVM method.

9. Conclusion

We developed a new two-step method for wavefront reconstruction from pyramid WFS data. The first step consists in the data preprocessing and transforms the pyramid sensor measurements into SH like data. As a second step we apply the CuReD algorithm, which reconstructs the unknown wavefront from SH measurements. The P-CuReD method provides the same or better reconstruction quality compared to the MVM method, but is significantly more efficient from a computational point of view. Both steps of our approach are computationally very cheap, the whole method has a linear complexity, is highly parallelizable and pipelinable. These features make our method especially attractive for usage in extreme AO.

Appendix A: Derivation of the Fourier Domain Filter in Case of Circular Modulation

In the circular modulation case, the linearized pyramid sensor measurements are given as

$$S_x^c(x, y) = -\frac{1}{\pi} \phi(x, y) * \frac{J_0(\alpha_\lambda x)}{x},$$

hence the FD filter function g_{pyr}^c is given as

$$\begin{aligned} \pi g_{\text{pyr}}^c(u) &= -\left(\mathcal{F}\left(\frac{J_0(\alpha_\lambda x)}{x}\right)\right)(u) \\ &= -(\mathcal{F}(J_0(\alpha_\lambda x)))(u) * \left(\mathcal{F}\left(\frac{1}{x}\right)\right)(u), \end{aligned}$$

where

$$\left(\mathcal{F}\left(\frac{1}{x}\right)\right)(u) = -i\pi \operatorname{sgn}(u),$$

and

$$(\mathcal{F}(J_0(\alpha_\lambda x)))(u) = \frac{1}{\pi u_{\text{mod}} \sqrt{1 - \frac{u^2}{u_{\text{mod}}^2}}} \Pi\left(\frac{u}{2u_{\text{mod}}}\right)$$

with Π being a characteristic function of the interval $[-1/2, 1/2]$

$$\Pi(u) := \begin{cases} 1, & |u| \leq \frac{1}{2}, \\ 0, & |u| > \frac{1}{2}. \end{cases}$$

Hence,

$$\begin{aligned} \pi g_{\text{pyr}}^c(u) &= \frac{i}{u_{\text{mod}}} \int_{-\infty}^{+\infty} \text{sgn}(u - u') \\ &\quad \times \frac{1}{\sqrt{1 - \frac{(u')^2}{u_{\text{mod}}^2}}} \Pi\left(\frac{u'}{2u_{\text{mod}}}\right) du' \\ &= \frac{i}{u_{\text{mod}}} \int_{-u_{\text{mod}}}^{u_{\text{mod}}} \frac{\text{sgn}(u - u')}{\sqrt{1 - \frac{(u')^2}{u_{\text{mod}}^2}}} du'. \end{aligned}$$

Using the substitution $v = u - u'$, we get

$$\pi g_{\text{pyr}}^c(u) = \frac{i}{u_{\text{mod}}} \int_{u-u_{\text{mod}}}^{u+u_{\text{mod}}} \frac{\text{sgn}(v)}{\sqrt{1 - \frac{(u-v)^2}{u_{\text{mod}}^2}}} dv.$$

On the interval $-u_{\text{cut}} < u < -u_{\text{mod}} < 0$, with the substitutions $w = u - v$ and $k = (w/u_{\text{mod}})$ we get

$$\begin{aligned} \pi g_{\text{pyr}}^c(u) &= -\frac{i}{u_{\text{mod}}} \int_{u-u_{\text{mod}}}^{u+u_{\text{mod}}} \frac{1}{\sqrt{1 - \frac{(u-v)^2}{u_{\text{mod}}^2}}} dv \\ &= -\frac{i}{u_{\text{mod}}} u_{\text{mod}} \int_{-1}^1 \frac{1}{\sqrt{1 - k^2}} dk = -2i \arcsin(1) \\ &= -i\pi. \end{aligned}$$

On the interval $0 < u_{\text{mod}} < u < u_{\text{cut}}$

$$\pi g_{\text{pyr}}^c(u) = \frac{i}{u_{\text{mod}}} \int_{u-u_{\text{mod}}}^{u+u_{\text{mod}}} \frac{1}{\sqrt{1 - \frac{(u-v)^2}{u_{\text{mod}}^2}}} dv = i\pi.$$

And on the interval $-u_{\text{mod}} \leq u \leq u_{\text{mod}}$ we get

$$\begin{aligned} \pi g_{\text{pyr}}^c(u) &= -\frac{i}{u_{\text{mod}}} \int_{u-u_{\text{mod}}}^0 \frac{1}{\sqrt{1 - \frac{(u-v)^2}{u_{\text{mod}}^2}}} dv \\ &\quad + \frac{i}{u_{\text{mod}}} \int_0^{u+u_{\text{mod}}} \frac{1}{\sqrt{1 - \frac{(u-v)^2}{u_{\text{mod}}^2}}} dv \\ &= -\frac{i}{u_{\text{mod}}} u_{\text{mod}} \int_{u/u_{\text{mod}}}^1 \frac{1}{\sqrt{1 - k^2}} dk \\ &\quad + \frac{i}{u_{\text{mod}}} u_{\text{mod}} \int_{-1}^{u/u_{\text{mod}}} \frac{1}{\sqrt{1 - k^2}} dk \\ &= 2i \arcsin(u/u_{\text{mod}}). \end{aligned}$$

Hence,

$$g_{\text{pyr}}^c(u) = \begin{cases} i \text{sgn}(u), & |u| > u_{\text{mod}}, \\ \frac{2i}{\pi} \arcsin(u/u_{\text{mod}}), & |u| \leq u_{\text{mod}}. \end{cases}$$

Appendix B: Derivation of the Space Domain Kernel in the Nonmodulated Case

The space domain kernel $p_{\text{sh/pyr}}^n$ is defined as the IFT of the Fourier domain SH/pyr transmission filter $g_{\text{sh/pyr}}^n$ given as

$$\begin{aligned} g_{\text{sh/pyr}}^n(u) &= 2\pi d|u|, \\ |u| \leq u_{\text{cut}} &= \begin{cases} -2\pi d u, & -u_{\text{cut}} \leq u < 0, \\ 2\pi d u, & 0 < u \leq u_{\text{cut}}, \end{cases} \end{aligned}$$

The kernel $p_{\text{sh/pyr}}^n$ is computed as

$$\begin{aligned} p_{\text{sh/pyr}}^n(x) &= (\mathcal{F}^{-1} g_{\text{sh/pyr}}^n)(x) \\ &= \int_{-u_{\text{cut}}}^{u_{\text{cut}}} g_{\text{sh/pyr}}^n(u) \exp(2\pi i x u) du \\ &= -2\pi d \underbrace{\int_{-u_{\text{cut}}}^0 u \exp(2\pi i x u) du}_{p_1^n(x)} \\ &\quad + 2\pi d \underbrace{\int_0^{u_{\text{cut}}} 2\pi d u \exp(2\pi i x u) du}_{p_2^n(x)}, \end{aligned}$$

where integration by parts gives

$$\begin{aligned} p_1^n(x) &= \frac{u_{\text{cut}}}{2\pi i x} \exp(-2\pi i x u_{\text{cut}}) + \frac{1}{4\pi^2 x^2} \\ &\quad - \frac{1}{4\pi^2 x^2} \exp(-2\pi i x u_{\text{cut}}), \end{aligned}$$

and

$$p_2^n(x) = \frac{u_{\text{cut}}}{2\pi ix} \exp(2\pi i x u_{\text{cut}}) + \frac{1}{4\pi^2 x^2} \exp(2\pi i x u_{\text{cut}}) - \frac{1}{4\pi^2 x^2}.$$

Therefore,

$$\begin{aligned} p_{\text{sh/pyr}}^n(x) &= -2\pi d p_1(x) + 2\pi d p_2(x) \\ &= -\frac{du_{\text{cut}}}{ix} \exp(-2\pi i x u_{\text{cut}}) \\ &\quad + \frac{d}{2\pi x^2} \exp(-2\pi i x u_{\text{cut}}) \\ &\quad + \frac{du_{\text{cut}}}{ix} \exp(2\pi i x u_{\text{cut}}) \\ &\quad + \frac{d}{2\pi x^2} \exp(2\pi i x u_{\text{cut}}) - \frac{d}{\pi x^2}. \end{aligned}$$

Using the equalities

$$\frac{\exp(ix) - \exp(-ix)}{2} = i \sin(x), \quad (\text{B1})$$

$$\frac{\exp(ix) + \exp(-ix)}{2} = \cos(x), \quad (\text{B2})$$

we get

$$p_{\text{sh/pyr}}^n(x) = \frac{2du_{\text{cut}}}{x} \sin(2\pi x u_{\text{cut}}) + \frac{d}{\pi x^2} \cos(2\pi x u_{\text{cut}}) - \frac{d}{\pi x^2}.$$

And using the trigonometric equality

$$\cos(x) = 1 - 2 \sin^2\left(\frac{x}{2}\right), \quad (\text{B3})$$

we obtain the kernel $p_{\text{sh/pyr}}^n$ as a sum of real-valued periodic functions

$$\begin{aligned} p_{\text{sh/pyr}}^n(x) &= \frac{2du_{\text{cut}}}{x} \sin(2\pi x u_{\text{cut}}) - \frac{2d}{\pi x^2} \sin^2(\pi x u_{\text{cut}}) \\ &= 4\pi d u_{\text{cut}}^2 \text{sinc}(2\pi x u_{\text{cut}}) \\ &\quad - 2\pi d u_{\text{cut}}^2 \text{sinc}^2(\pi x u_{\text{cut}}). \end{aligned} \quad (\text{B4})$$

Appendix C: Derivation of the Space Domain Kernel in Case of Linear Modulation

The space domain kernel $p_{\text{sh/pyr}}^l$ is defined as the IFT of the Fourier domain SH/pyr transmission filter $g_{\text{sh/pyr}}^l$ given as

$$g_{\text{sh/pyr}}^l(u) = \begin{cases} -2\pi d u, & u < -u_{\text{mod}}, \\ 2\pi d u_{\text{mod}}, & -u_{\text{mod}} \leq u \leq u_{\text{mod}}, \\ 2\pi d u, & u > u_{\text{mod}}. \end{cases}$$

The kernel $p_{\text{sh/pyr}}^l$ can be written as a sum of three terms

$$\begin{aligned} p_{\text{sh/pyr}}^l(x) &= (\mathcal{F}^{-1} g_{\text{sh/pyr}}^l)(x) \\ &= \int_{-u_{\text{cut}}}^{u_{\text{cut}}} g_{\text{sh/pyr}}^l(u) \exp(2\pi i x u) du \\ &= -p_1^l(x) + p_2^l(x) + p_3^l(x), \end{aligned}$$

where p_2 is an elementary integral

$$\begin{aligned} p_2^l(x) &= 2\pi d u_{\text{mod}} \int_{-u_{\text{mod}}}^{u_{\text{mod}}} \exp(2\pi i x u) du \\ &= \frac{du_{\text{mod}}}{ix} \exp(2\pi i x u_{\text{mod}}) - \frac{du_{\text{mod}}}{ix} \exp(-2\pi i x u_{\text{mod}}), \end{aligned}$$

and the terms p_1 and p_3 are integrated by parts as

$$\begin{aligned} p_1(x) &= 2\pi d \int_{-u_{\text{cut}}}^{-u_{\text{mod}}} u \exp(2\pi i x u) du \\ &= -\frac{du_{\text{mod}}}{ix} \exp(-2\pi i x u_{\text{mod}}) \\ &\quad + \frac{du_{\text{cut}}}{ix} \exp(-2\pi i x u_{\text{cut}}) \\ &\quad + \frac{d}{2\pi x^2} \exp(-2\pi i x u_{\text{mod}}) - \frac{d}{2\pi x^2} \exp(-2\pi i x u_{\text{cut}}), \end{aligned}$$

$$\begin{aligned} p_3(x) &= 2\pi d \int_{u_{\text{mod}}}^{u_{\text{cut}}} u \exp(2\pi i x u) du \\ &= \frac{du_{\text{cut}}}{ix} \exp(2\pi i x u_{\text{cut}}) - \frac{du_{\text{mod}}}{ix} \exp(2\pi i x u_{\text{mod}}) \\ &\quad + \frac{d}{2\pi x^2} \exp(2\pi i x u_{\text{cut}}) - \frac{d}{2\pi x^2} \exp(2\pi i x u_{\text{mod}}). \end{aligned}$$

Collecting the three terms and using the equalities (B1) and (B2), we obtain the kernel $p_{\text{sh/pyr}}^l$ as a sum of real-valued periodic functions

$$\begin{aligned} p_{\text{sh/pyr}}^l(x) &= \frac{2du_{\text{cut}}}{x} \sin(2\pi x u_{\text{cut}}) - \frac{d}{\pi x^2} \cos(2\pi x u_{\text{mod}}) \\ &\quad + \frac{d}{\pi x^2} \cos(2\pi x u_{\text{cut}}). \end{aligned}$$

Using the trigonometric equality (B3), we finally obtain the kernel $p_{\text{sh/pyr}}$ as a sum of (squared) sinc functions

$$\begin{aligned} p_{\text{sh/pyr}}^l(x) &= 4\pi d u_{\text{cut}}^2 \text{sinc}(2\pi x u_{\text{cut}}) \\ &\quad + 2\pi d u_{\text{mod}}^2 \text{sinc}^2(\pi x u_{\text{mod}}) \\ &\quad - 2\pi d u_{\text{cut}}^2 \text{sinc}^2(\pi x u_{\text{cut}}). \end{aligned} \quad (\text{C1})$$

This research was done within the project “Mathematical Algorithms and Software for E-ELT Adaptive Optics,” which is funded by the Austrian Federal Ministry of Science and Research. We would like to thank Mariya Zhariy from Software Competence Center Hagenberg (SCCH) and Christophe Vérinaud from Laboratoire d’Astrophysique, Observatoire de Grenoble (LAOG) for discussions concerning the pyramid WFS models and simulations. We thank Miska Le Louarn from ESO for help with OCTOPUS and fruitful discussions. We also thank Andrii Prylepa from Center for Surface and Nanoanalytics (ZONA) for providing us a graphical scheme of the pyramid WFS.

References

1. V. Korhikoski and C. Verinaud, “Extreme adaptive optics simulations for EPICS,” in *First AO4ELT Conference—Adaptive Optics for Extremely Large Telescopes*, T. F. Y. Clénet, J.-M. Conan, and G. Rousset, eds. (EDP Sciences, 2010), p. 03007.
2. F. Roddier, *Adaptive Optics in Astronomy* (Cambridge University, 1999).
3. R. Ragazzoni, “Pupil plane wavefront sensing with an oscillating prism,” *J. Mod. Opt.* **43**, 289–293 (1996).
4. R. Ragazzoni, E. Diolaiti, and E. Vernet, “A pyramid wavefront sensor with no dynamic modulation,” *Opt. Commun.* **208**, 51–60 (2002).
5. R. Ragazzoni and J. Farinato, “Sensitivity of a pyramidal wave front sensor in closed loop adaptive optics,” *Astron. Astrophys.* **350**, L23–L26 (1999).
6. S. Esposito and A. Riccardi, “Pyramid wavefront sensor behavior in partial correction adaptive optic systems,” *Astron. Astrophys.* **369**, L9–L12 (2001).
7. S. Esposito, A. Riccardi, and O. Feeney, “Closed-loop performance of pyramid wavefront sensor,” *Proc. SPIE* **4034**, 184–189 (2000).
8. M. Feldt, D. Peter, S. Hippler, T. Henning, J. Aceituno, and M. Goto, “PYRAMIR: first on-sky results from an infrared pyramid wavefront sensor,” *Proc. SPIE* **6272**, 627218 (2006).
9. D. Peter, M. Feldt, T. Henning, S. Hippler, J. Aceituno, L. Montoya, J. Costa, and B. Dorner, “PYRAMIR: exploring the on-sky performance of the world’s first near-infrared pyramid wavefront sensor,” *Publ. Astron. Soc. Pac.* **122**, 63–70 (2010).
10. V. Korhikoski, C. Vérinaud, M. Le Louarn, and R. Conan, “Comparison between a model-based and a conventional pyramid sensor reconstructor,” *Appl. Opt.* **46**, 6176–6184 (2007).
11. C. Vérinaud, “On the nature of the measurements provided by a pyramid wave-front sensor,” *Opt. Commun.* **233**, 27–38 (2004).
12. A. Burvall, E. Daly, S. R. Chamot, and C. Dainty, “Linearity of the pyramid wavefront sensor,” *Opt. Express* **14**, 11925–11934 (2006).
13. D. W. Phillion and K. Baker, “Two-sided pyramid wavefront sensor in the direct phase mode,” *Proc. SPIE* **6274**, 627228 (2006).
14. F. Quirós-Pacheco, C. Correia, and S. Esposito, “Fourier transform-wavefront reconstruction for the pyramid wavefront sensor,” in *First AO4ELT Conference—Adaptive Optics for Extremely Large Telescopes*, T. F. Y. Clénet, J.-M. Conan, and G. Rousset, eds. (EDP Sciences, 2010), p. 07005.
15. M. Rosensteiner, “Cumulative reconstructor: fast wavefront reconstruction algorithm for extremely large telescopes,” *J. Opt. Soc. Am. A* **28**, 2132–2138 (2011).
16. M. Rosensteiner, “Wavefront reconstruction for extremely large telescopes via CuRe with domain decomposition,” *J. Opt. Soc. Am. A* **29**, 2328–2336 (2012).
17. M. Zhariy, A. Neubauer, M. Rosensteiner, and R. Ramlau, “Cumulative wavefront reconstructor for the Shack–Hartman sensor,” *IPI* **5**, 893–913 (2011).
18. J. LeDue, L. Jolissant, J.-P. Véran, and C. Bradley, “Calibration and testing with real turbulence of a pyramid sensor employing static modulation,” *Opt. Express* **17**, 7186–7195 (2009).
19. M. Le Louarn, C. Vérinaud, V. Korhikoski, N. Hubin, and E. Marchetti, “Adaptive optics simulations for the European extremely large telescope,” *Proc. SPIE* **6272**, 627234 (2006).
20. A. Garcia-Rissmann and M. Le Louarn, “SCAO simulation results with a pyramid sensor on an ELT-like telescope,” in *First AO4ELT Conference—Adaptive Optics for Extremely Large Telescopes*, T. F. Y. Clénet, J.-M. Conan, and G. Rousset, eds. (EDP Sciences, 2010), p. 03011.